Enhanced removal of dissolved effluent organic matter in wastewater using lignin-based biochar supported Fe–Cu bimetallic oxide catalyst

Journal of *Marine Science and Engineering*

MDPI

Article

Enhanced Removal of Dissolved Effluent Organic Matter in Wastewater Using Lignin-Based Biochar Supported Fe–Cu Bimetallic Oxide Catalyst

Wenpeng Wang [1], Fanlong Kong [1,2], Huazhen Wu [1], Chunyan Zhai [1], Yang Li [1], Sen Wang [1,2,*] and Hong Yang [3,*]

[1] College of Environmental Science and Engineering, Qingdao University, Qingdao 266071, China; wangsen@qdu.du.cn (W.W.); kongfanlong@126.com (F.K.); 15063071312@163.com (H.W.); zhaichunyan2023@126.com (C.Z.); 15966127909@163.com (Y.L.)
[2] Carbon Neutrality and Eco-Environmental Technology Innovation Center of Qingdao, Qingdao 266071, China
[3] Department of Geography and Environmental Science, University of Reading, Reading RG6 6AB, UK
* Correspondence: wangsen@qdu.edu.cn (S.W.); h.yang4@reading.ac.uk (H.Y.)

Abstract: The effluent discharged from wastewater treatment facilities frequently enters the ocean, posing a considerable threat to the health of marine life and humans. In this paper, an alkali lignin-based biochar-loaded modified Fe–Cu catalyst (FeCu@BC) was prepared to remove soluble microbial products (SMP) from secondary effluent as disinfection by-products precursors at ambient temperature and pressure. The humic acid (HA) was taken as the representative substance of SMP. The results showed that the maximum removal efficiency of HA reached 93.2% when the FeCu@BC dosage, pH, initial HA concentration, and dissolved oxygen concentration were 5.0 g/L, 7, 100 mg/L, and 1.75 mg/L, respectively. After three cycles, the removal efficiency of HA could be maintained at more than 70%. The quenching experiments and electron spin resonance (EPR) results showed that •OH and $^1O_2$ were involved in the degradation of HA in the FeCu@BC catalyst reaction system, with $^1O_2$ playing a dominant role. Theoretical calculations confirmed that •OH and $^1O_2$ were more prone to attack the C=O bond of the side chain of HA. After processing by the FeCu@BC catalyst, the yield of chlorinated disinfection by-products from secondary effluent had decreased in an obvious manner. This study provides a new solution to efficiently solve the problem of chlorinated disinfection by-products from HA.

Keywords: catalytic wet air oxidation; secondary effluent organic matter; soluble microbial products; DFT calculation; toxicity assessment

Citation: Wang, W.; Kong, F.; Wu, H.; Zhai, C.; Li, Y.; Wang, S.; Yang, H. Enhanced Removal of Dissolved Effluent Organic Matter in Wastewater Using Lignin-Based Biochar Supported Fe–Cu Bimetallic Oxide Catalyst. *J. Mar. Sci. Eng.* **2024**, *12*, 183. https://doi.org/10.3390/jmse12010183

Academic Editor: Ryan J.K. Dunn

Received: 23 December 2023
Revised: 13 January 2024
Accepted: 16 January 2024
Published: 19 January 2024

1. Introduction

Due to the rapid population growth and industrial development, massive wastewater treatment plants have been constructed to treat the increasing discharge of wastewater around the world, most of which use biological treatment processes [1,2]. The secondary effluent after biological treatment usually contains soluble microbial products (SMP), natural organic matter (NOM), as well as the heterogeneous mixtures of synthetic organic constituents and their intermediates [3]. Among these dissolved matters, SMP was considered to be the main component of the secondary effluent organic matter (EfOM), which accounted for about 50–60% of the tdataotal chemical oxygen demand (COD) of wastewater [4]. To maintain ecological safety and protect public health from infectious waterborne diseases, the wastewater after biological treatment must be disinfected before discharge. Due to its low cost and process simplicity, sodium hypochlorite is one of the most commonly used disinfectants [5,6]. However, chlorate might react with functional groups in SMP, such as carboxyl, aryl, amino, and hydroxyl, to form disinfection by-products (DBPs), e.g., haloacetic acids (HAAs), trihalomethanes (THMs), etc. [7,8]. In coastal cities, the effluent from wastewater treatment plants is usually discharged into the sea along rivers or

pipelines, posing a high risk to marine organisms and human health [9]. Compared to the treatment of DBPs, SMP removal before chlorination is more economical, environmentally friendly, and effective [10]. However, traditional processes such as coagulation, sedimentation, and filtration are unable to effectively remove SMP after biological treatment, which also presents shortcomings such as high coagulant consumption, filter clogging, and membrane contamination [11,12]. Seeking an economical and environmentally friendly method for the removal of SMP has become an urgent challenge to reduce the generation of disinfection by-products and improve the quality of tailwater.

At present, a variety of technologies have been used to remove SMP, such as biological treatment technologies (biofilters, constructed wetlands, oxidation ditches, etc.), physical treatment technology (activated carbon adsorption, coagulation sedimentation, membrane filtration, etc.) [13,14], and advanced oxidation processes (AOPs), e.g., photocatalysis, fenton, electrochemistry, ozone catalysis, etc. [15–17]. Due to its chemical stability, SMP is extremely inefficient at biodegradation and might be produced again by microorganisms. In addition, the physical treatment could only transfer pollutants from the water phase to the surface of the solid adsorbent, with the risk of secondary release. Recently, AOPs have attracted widespread concern, because they can quickly adsorb SMP and convert it into smaller compounds, such as CO_2 and H_2O [18,19]. As a typical AOPs technology, catalytic wet oxidation (CWAO) has the advantages of wide application range, high efficiency, and low energy consumption, with good removal effect on refractory organics such as humic acid (HA, the main component of SMP), phenol, and natural organics [20,21]. Cai et al. [22] reported that 91% of HA and 90% of organic carbon in organic wastewater containing HA were removed within 10 min at 90 °C in a $TiZrO_4$@5%CuSA system. Unfortunately, most CWAO is conducted under high temperature (120–320 °C) and high pressure (0.5–20 MPa), increasing the costs of operation and maintenance as well as causing the problem of metal ion precipitation [23,24], all of which limit its practical application. Therefore, the development of catalysts with high activity at room temperature and pressure is the key to removing SMP in secondary effluent by CWAO.

As a transition metal, iron (Fe) is one of the most abundant elements on earth. Due to the advantages of low cost and easy access, Fe has been widely used in the preparation of catalyst materials, such as nano-zero-valent iron (nZVI) [25], Fe_2O_3 [26], and FeS [27]. However, the low catalytic activity, poor stability, and poor recyclability limit the application of the above Fe-based catalytic materials to the removal of SMP from secondary effluent. In recent years, heterogeneous catalysts have been widely studied due to their excellent catalytic activity and durability [28,29], with bimetallic oxides with good catalytic effect, many cycles, and good stability becoming a research hotspot [30]. By incorporating copper (Cu) into the surface of nano- or micro-sized iron oxides (Fe–Cu bimetallic oxide), a larger specific surface area and more ductility chains would be obtained, which could avoid the rapid corrosion of Fe, ensure the long-term release of iron ions, and improve the reduction capacity of Fe and the utilization of organic matter by microorganisms [31]. Because of its inherent high surface energy and low specific surface area, the catalyst is easy to aggregate, resulting in a decrease in the number of active centers and catalytic efficiency. Researchers have tried to introduce carrier materials to prevent the nanocatalyst/Fe–Cu bimetallic oxide from coming together. For example, biochar (BC), with its low cost, large specific surface area, and rich surface functional groups [32], can increase the contact probability between organic pollutants and active free radicals by mesoporous structure and high surface areas, and adsorb organic matter in water [33]. Alkali lignin (AL) is a major by-product of the paper industry, which accounts for 85% of global lignin production [34]. However, only 5% of AL is utilized, most of which is used as fuel for energy recovery or for the manufacturing of chemicals, leading to the waste of valuable lignin resources and to environmental pollution [35]. In view of the abundant mesoporous structure, stable graphite skeleton, strong electrical conductivity, and rich functional groups, the use of alkaline lignin-based BC as a carrier has become an effective way to improve the electron transfer capacity and adsorption capacity of the Fe–Cu bimetallic oxide catalyst during the

CWAO process. However, the mechanism of an alkali lignin-based BC-supported FeCu@BC catalyst and its effect on SMP removal in secondary effluent are still largely unknown.

To fill the knowledge gap, an alkali lignin-based BC-supported Fe–Cu bimetallic oxide was prepared by pyrolysis and used to solve the problem of disinfection by-products produced by humic acid (HA)—the main component of SMP—during chlorine disinfection. The main objectives of this study are: (1) to prepare and screen the appropriate FeCu@BC catalyst with the excellent HA removal performance; (2) to explore the mechanism used by the alkali lignin-based BC-supported FeCu@BC catalyst for the removal of HA using density functional theory (DFT); (3) to investigate the generation of chlorinated disinfection by-products before and after treatment by the alkali lignin-based BC-supported FeCu@BC catalyst. The finding of this study can provide a new way to reduce the production of DBPs in the effluent of wastewater treatment plants.

2. Materials and Methods

2.1. Materials and Reagents

$FeCl_3 \cdot 6H_2O$, HA, and $CuCl_2 \cdot 2H_2O$ were purchased from Sinopharm Chemical Reagent Co., Ltd. (Shanghai, China). Zeolite powder (200 mesh) and lignin (100–200 mesh) were purchased from Hengxin Water Purification Technology Co., Ltd. (Shenzhen, China) and Dongming Chenyuan Wood Industry Co., Ltd. (Heze, China), respectively.

A total of 1.00 g of HA and 0.40 g of NaOH was dissolved and diluted with 1 L deionized water, and then stirred rapidly for 12 h. After using 0.45 μm membrane filtration, 1 g/L of HA reserve solution was obtained [36]. The pH of the solution was adjusted to 7.00 ± 0.02 using 1 mol/L of HCl solution or NaOH solution before the experiment.

The experimental water samples were collected from the secondary effluent of Qingdao maidao wastewater plant, and the sampling location was the effluent of the biofilter (before disinfection). The water samples were collected using a sampler, and then poured into a pre-cleaned 25 L bucket and transported back to the laboratory immediately. The water samples were filtered through a 0.45 μm membrane and stored in a dark place at 4 °C for subsequent experiments. The detailed parameters of water samples, including Total Suspended Solids (TSS), pH, Biochemical Oxygen Demand (BOD_5), conductivity, and ions are presented in Table 1.

Table 1. The detailed parameters of water samples.

Parameters	Average Value	Unit (mg/L)
COD	48.21	mg/L
BOD_5	13.65	mg/L
TP	0.18	mg/L
TN	12.32	mg/L
NH_4^+-N	5.62	mg/L
TSS	12.60	mg/L
Cl^-	46.34	mg/L
NO_3^{2-}	6.47	mg/L
SO_4^{2-}	36.52	mg/L
Conductivity	1952	μS/cm
pH	7.62	-

2.2. Preparation of the Lignin-Based BC-Supported FeCu@BC Catalyst

A one-step pyrolysis method was used to synthesize the FeCu@BC catalyst. The detailed experimental procedure was as follows. Firstly, 6.5 g of $FeCl_3 \cdot 6H_2O$ and 1.5 g of $CuCl_2 \cdot 2H_2O$ was dissolved into 30 mL of distilled water. Then, the solution was titrated to pH = 7 with 12 mol/L of ammonia and mixed thoroughly. Subsequently, 15.0 g of alkali lignin was added and magnetically stirred for 1 h. The resulting mixture was dried at 105 °C overnight. The dried solid was ground to a fine powder using an onyx mortar and loaded into a muffle furnace for pyrolysis at the given temperatures (500 °C) with a nitrogen flow rate of 200 mL/min, a heating rate of 10 °C/min, and a retention time of 1.5 h. The pyrolyzed samples were rinsed alternately with ethanol and purified water to

remove adhering tarry organic and inorganic matter and washed to pH = 7. Finally, after vacuum drying at 60 °C, the samples were ground and screened through 100–160 mesh for subsequent characterization and experiments.

2.3. Characterization of the Lignin-Based BC-Supported FeCu@BC Catalyst

The morphology and microstructure of the lignin-based BC-supported FeCu@BC catalyst were studied by using scanning electron microscopy (SEM, FEG 250, FEI-Quanta, EUG, Hillsboro, OR, USA) and energy dispersive X-ray spectroscopy (EDS) elemental mapping. The mineralogical composition of the materials was analyzed using X-ray diffractometer (XRD, D8 Advance, Bruker, Bremen, Germany). Fourier transform infrared spectroscopy (FT-IR, NEXUS-670, Thermo Nicolet, Thermo Scientific, Waltham, MA, USA) was used for the functional groups on the material surface. X-ray photoelectron spectroscopy (XPS, K-alpha, Thermo Scientific, Waltham, MA, USA) was used to study the elemental composition and for the quantification of different chemical states. The specific surface areas of the FeCu@BC catalyst were measured by specific surface area and porosity analyzer (BET, TriStar II 3020, Micromeritics Instruments Corporation, Norcross, GA, USA).

2.4. Batch Experiment

2.4.1. Effect of Catalyst Dosage on HA Removal

The effect of catalyst dosage (1 g/L, 3 g/L, 5 g/L, 7 g/L, and 10 g/L) on HA removal by the FeCu@BC catalyst was studied. The diluted HA solution (200 mL, 100 mg/L) was transferred to a conical flask, and materials of different weights were added separately to the conical flask, sealed, and oscillated in a thermostatic oscillator (150 rpm, 25 °C). After 48 h, the solution was filtered and the concentration of HA was measured.

2.4.2. Effect of pH on HA Removal

The effect of the initial pH (3–11) on the HA removal performance of the FeCu@BC catalyst was investigated. The diluted HA solution (200 mL, 100 mg/L) was transferred to a conical flask and titrated with hydrochloric acid and sodium hydroxide solution (0.1 mol/L) to 3–11. The shaking conditions and the determination of HA concentration were the same as those described in Section 2.4.1.

2.4.3. Effect of Initial Concentration on HA Removal

The effect of the initial concentration (10 mg/L, 20 mg/L, 50 mg/L, and 100 mg/L) of the FeCu@BC catalyst on HA removal was investigated. A total of 200 mL of HA solution (10 mg/L, 20 mg/L, 50 mg/L, and 100 mg/L) was transferred to the conical flask, and different materials were added to the conical flask separately. The shaking conditions and the determination of HA concentration were the same as those described in Section 2.4.1.

2.4.4. Effect of Inorganic Ions on HA Removal

In view of the widespread presence of Cl^-, NO_3^-, NH_4^+, SO_4^{2-}, and PO_4^{3-} in secondary effluent, the effects of different inorganic ion concentrations on the HA removal performance of the FeCu@BC catalyst were studied, and lignin BC and an unsupported carrier were used as controls (Table 2). The shaking conditions, HA dosage, and the determination of HA concentration were the same as those described in Section 2.4.1.

Table 2. The concentration gradients of inorganic ions and the corresponding reagents.

Inorganic Ions	Concentration Gradients (mg/L)				Reagent
Cl^-	5	10	20	50	NaCl
NO_3^{2-}	1	2	5	10	$NaNO_3$
NH_4^+	0.5	1	2	5	NH_4Cl
SO_4^{2-}	5	10	20	50	Na_2SO_4
PO_4^{3-}	0.1	0.2	0.5	1.0	Na_2PO_4

2.4.5. Effect of Dissolved Oxygen Concentration on HA Removal

Considering the presence of a certain concentration of dissolved oxygen (DO) in secondary effluent (before disinfection), the effects of different air flow rates (0 L/min, 5 L/min, 10 L/min, and 50 L/min) on HA removal by the FeCu@BC catalyst were analyzed. The DO was measured in situ by a multiparameter (Multi 3630, WTW, MUC, Troistedt, Germany). The vibration conditions, HA dosage, and concentration were determined as described in Section 2.4.1.

2.4.6. Reusability and Stability of the FeCu@BC Catalyst

The HA was pumped into the fixed-bed column (length = 8 cm, inner diameter = 2 cm) by a peristaltic pump in a downward inlet and upward outlet mode (Figure 1). The fixed-bed column was filled with prepared FeCu@BC catalyst (height = 4 cm), the concentration of HA inlet water was 50 mg/L, and the hydraulic retention time was 6 h. The experimental procedure simulated a fixed-bed catalytic run to carry out reproducible practicality and stability experiments. The experimental procedure simulated a fixed-bed catalytic run to carry out reproducibility and stability experiments. Precipitation experiments were carried out on the concentration of HA, and metal ions precipitated at the end of the experiment. The reacted material was placed in a conical flask and 150 mL of hydrochloric acid solution (0.1 mol/L) was added. The vibration conditions, HA dosage, and concentration were determined as described in Section 2.4.1.

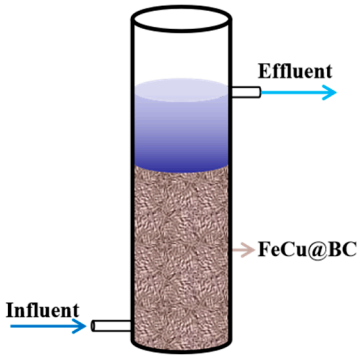

Figure 1. Fixed-bed catalytic reactor.

2.5. Sample Acquisition and Analysis

2.5.1. Treatment and Determination of Dissolved Organic Matter

The HA concentration in the solution was determined by colorimetric analysis at 460 nm. $A_{254}/A_{254'}$ was used to represent the change in solution Uv_{254} during the reaction, and the calculation formula was as follows:

$$A_{254}/A_{254'} = \frac{Uv_{254}}{Uv_{254'}} \quad (1)$$

E_2/E_3 represents the molecular weight change relationship, and the calculation formula was as follows:

$$E_2/E_3 = \frac{Uv_{254}}{A_{365}} \quad (2)$$

2.5.2. 3D-EEM Analysis

The three-dimensional fluorescence excited emission matrix (3D-EEM) of the water sample was measured with a fluorescence spectrophotometer (F-4600, Hitachi, Tokyo, Japan), with ultra-pure water as a blank. The range of emission wavelengths (Em) and excitation wavelengths (Ex) was 200–600 nm and 200–600 nm, respectively, and the scanning interval, scanning slit, and scanning speed were 5 nm, 10 nm, and 2400 nm/min, respectively.

2.5.3. Quenching Experiment

In order to investigate the role of reactive oxygen species (ROS) in the FeCu@BC system, quenching experiments were carried out with methanol (MeOH), tert-butanol (TBA), n-butanol (NBA), and furfuryl alcohol (FFA) as quenchers. The quencher dosage used in the quenching experiment was 1.5 mol/L. At the same time, the electron paramagnetic resonance (EPR, Bruker EMX PLUS, Bremen, Germany) spectrometer with DMPO or TEMP as a capture agent was used to capture the ROS.

2.5.4. DBPs Determination

To determine DBPs, 5 mL of sodium hypochlorite solution (30%) was added to raw and treated water samples. The mixture was stored at room temperature in darkness for 24 h, and then the THMs and HAAs were extracted with MTBE. The extraction methods were slightly modified from the EPA methods 331.0 and 557.0 [37]. HAAs were esterified with methanol before instrumental analysis. The DBPs concentrations were determined by UPLC-MS (1290/Q-TOF 6550, Agilent, Santa Clara, CA, USA).

2.5.5. Other Analytical Measurements

The COD, NO_2^--N, NH_4^+-N, NO_3^--N, and TP were determined following the Chinese National Environmental Protection Agency Water and Wastewater Monitoring Methods [38]. The pH was measured using a pH/mV meter (PHS-3CW, INESA Scientific Instrument Co., Ltd., Shanghai, China). The Cu (II) and Fe (II) were determined by sodium diethyldithiocarbamate spectrophotometry and phenanthroline spectrophotometry [39].

2.6. DFT Calculation Methods

DFT calculations were carried out using the Gaussian 16 software. The B3LYP functional was adopted for all calculations in combination with the D3BJ dispersion correction. In geometry optimization and frequency calculations, the 6–31 G basis set was used. The figures were drawn using the Multiwfn programme [40].

2.7. Data Analysis

The Origin 2022b software was used to analyze and plot experimental data. Matlab 2018 was used to plot 3D-EEM spectra that can remove Raman scattering and Rayleigh scattering, as well as perform normalization processing. Statistical analyses of all experimental data were performed using SPSS 26.0 (SPSS, Inc., Chicago, IL, USA), and significance analysis was performed by analysis of variance (ANOVA) (statistical significance level $p < 0.05$).

3. Results and Discussion

3.1. Composition and Characterization of FeCu@BC

3.1.1. Surface Morphology and Elemental Analysis of FeCu@BC

The SEM images of BC and of the FeCu@BC catalyst before and after the reaction are presented in Figure 2. The surface of BC was rough, loose, and porous, providing favorable conditions for the loading of Fe–Cu bimetallic oxides (Figure 2a). The EDS results show that the surface elements of BC were dominated by C and O, where the higher Na and Cl elements might be due to raw material composition. As shown in Figure 2b, the surface of the FeCu@BC catalyst had differently sized and unevenly distributed protrusions. After reaction with HA, the pores on the surface of the FeCu@BC catalyst decreased and the agglomerates increased. This was possibly caused by the fact that HA was adsorbed on the material surface and filled the holes (Figure 2c). The decreasing contents of Fe and Cu on the FeCu@BC catalyst suggest that the FeCu@BC catalyst reacted with HA.

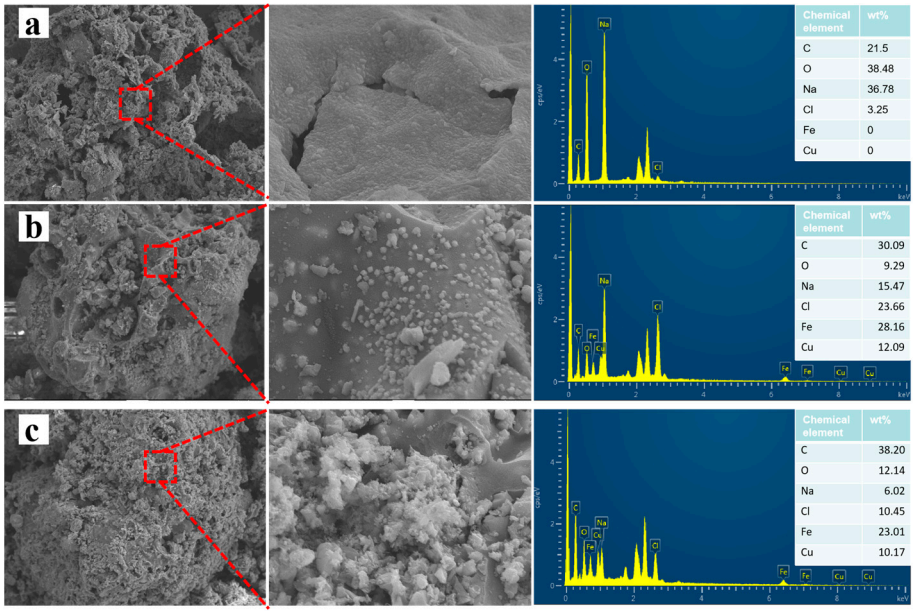

Figure 2. Surface morphologies and EDS results of BC (**a**), FeCu@BC catalysts before the reaction with HA (**b**) and FeCu@BC catalysts after reaction with HA (**c**).

3.1.2. BET Analysis

The size of the specific surface area of the adsorption material was an important factor affecting its adsorption effect. Figure 3a,b shows the N_2 adsorption–desorption isotherms and pore size distributions before and after HA removal by the FeCu@BC catalyst. The adsorption isotherm of the FeCu@BC catalyst before the removal of HA conformed to the characteristics of the type IV isotherm with mid-range adsorption lag, and the average pore size was below 10 nm, indicating that the FeCu@BC catalyst was a mesoporous material [41]. Before and after HA removal by the FeCu@BC catalyst, the specific surface and the average resolved pore diameters were 56.65 m^2/g and 35.23 m^2/g and 9.45 nm and 4.76 nm, respectively. This result might be attributed to the fact that the porous surfaces of the FeCu@BC catalysts were slightly corroded after treating HA, and the adsorbed substances blocked the pores and reduced the average pore size [42,43].

3.1.3. XRD Analysis

Figure 3c shows the characteristic peaks of Fe^0, Fe_3O_4, FeO, Cu^0, and CuO. The peaks at 2θ = 44.7° and 65.1° were attributed to Fe^0 [42], and those at 30.1°, 35.4°, 53.4°, and 57.0° were attributed to magnetite Fe_3O_4 [44]. The peaks at 43.3°, 50.4°, and 74.1° were attributed to Cu^0, and those at 35.9° were attributed to FeO [45]. In addition, the graphite-002 crystal peaks at 2θ (25° and 35°) suggest that BC with a graphitized structure was formed during pyrolysis [46].

3.1.4. FTIR Analysis

FTIR spectra were used to better understand the surface groups of the FeCu@BC catalysts (Figure 3d). Before reaction, BC and FeCu@BC had absorption peaks at 3415 cm^{-1}, 1596 cm^{-1}, and 1130 cm^{-1} caused by O–H, C=C and C–O–C stretching, respectively. The absorption peaks of BC at 1443 cm^{-1} and 2921 cm^{-1} were due to the formation of aromatic C=C backbone stretching vibrations and symmetric and asymmetric stretching of C–H. The stretching vibration peaks of Fe–O and Cu–O at 530 cm^{-1} and 444 cm^{-1} indicate that the Fe and Cu were successfully loaded onto the BC surface to form the FeCu@BC catalyst. Meanwhile, more -OH groups appeared on the surface of the FeCu@BC catalyst, a phenomenon that is conducive to the removal of HA by the FeCu@BC catalyst [41].

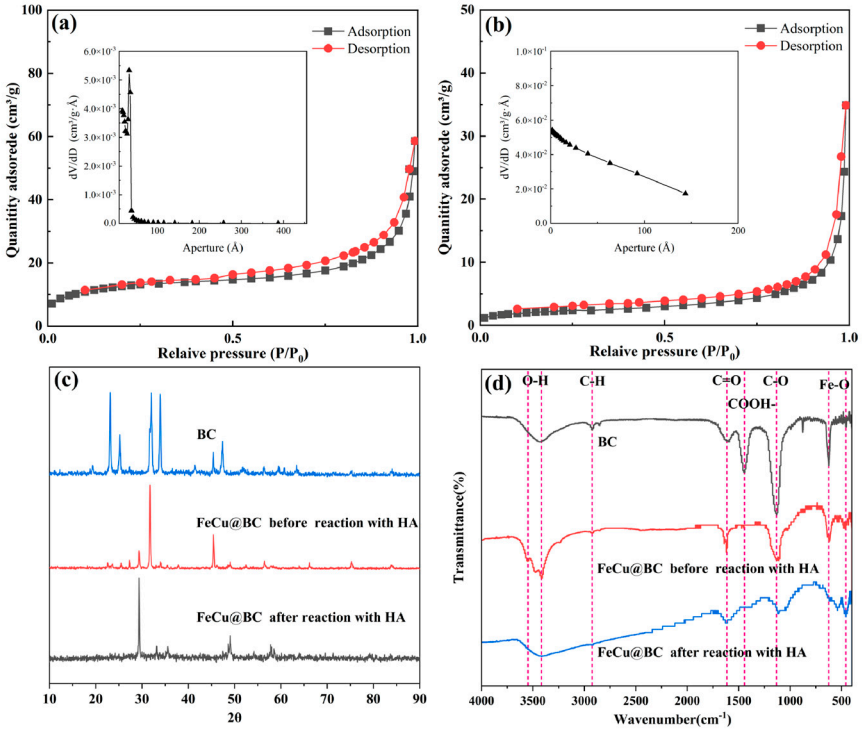

Figure 3. N_2 adsorption–desorption isotherms and pore size distributions of the FeCu@BC catalysts before (**a**) and after (**b**) reaction with HA. XRD patterns (**c**) and FTIR spectra of the FeCu@BC catalyst (**d**).

3.1.5. XPS Analysis

The elemental composition and valence states of FeCu@BC catalysts were characterized using XPS. The surface elements of the FeCu@BC catalyst include C, O, Fe, and Cu (Figure 4a), consistent with the results from the EDS (Figure 2). As shown in Figure 4b, before the reaction of the FeCu@BC catalyst, three peaks at 284.80 eV, 285.81 eV, and 288.22 eV corresponded to C–C, C–O, and C=O, respectively [31]. The peaks near 530.61 eV, 534.86 eV, and 535.96 eV were attributed to M–O, C=O, and C–O, respectively (Figure 4c). In the Cu 2p spectra (Figure 4d), the peaks at 932.13 eV and 952.00 eV corresponded to Cu^0 2p3/2 and 2p1/2, respectively. The peaks at 942.34 eV were likely attributable to Cu (II) species (i.e., CuO). In the Fe 2p spectra of the FeCu@BC catalyst (Figure 4e), the fitted peaks at 711.44 eV and 714.33 eV were ascribed to Fe (II) 2p1/2 and 2p3/2, and those at 717.50 eV and 722.79 eV were ascribed to Fe (III) 2p1/2 and 2p3/2, respectively [34]. The above results further prove that Fe and Cu were successfully loaded onto BC and existed mainly in the form of Fe_3O_4, FeO, CuO, and Cu^0, consistent with XRD results.

3.2. Removal Performance of FeCu@BC for HA under Different Reaction Conditions

3.2.1. FeCu@BC Catalyst Dosage

The HA removal efficiencies under different FeCu@BC dosages are shown in Figure 5a. It was found that the HA removal efficiencies increased from 43.3% to 57.6% and 83.7%, with the increase in FeCu@BC dosages from 1.0 g/L to 3.0 g/L and 5.0 g/L (60 min). This result might be attributed to the fact that a higher catalyst dosage could provide more active sites and accelerate the generation of free radicals to improve HA removal. However, when the FeCu@BC dosages were further increased to 7 g/L and 10 g/L, the HA removal efficiency was only 1.9% and 2.3% higher than that at 5.0 g/L FeCu@BC (360 min), respectively. Considering the treatment effect and economy, the FeCu@BC with 5.0 g/L dosage was adopted in the subsequent experiments.

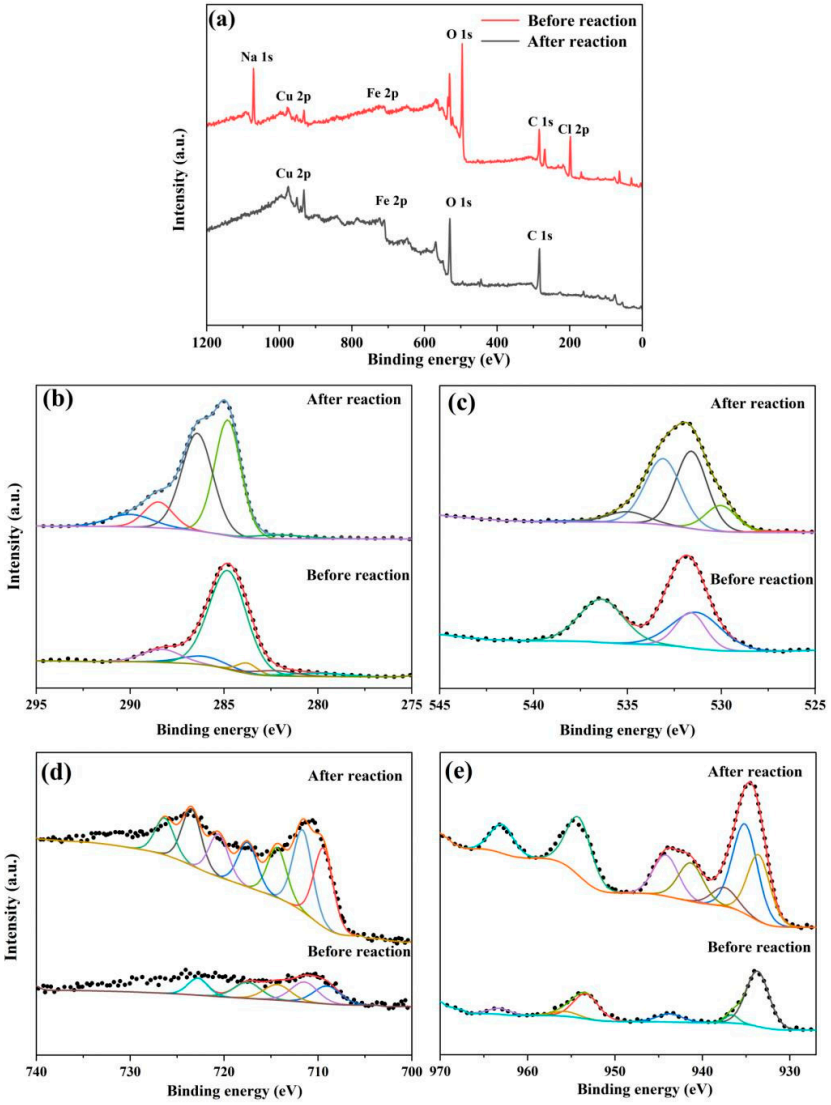

Figure 4. FeCu@BC XPS spectra before and after HA removal. (**a**) Total XPS spectrum, (**b**) C(1s), (**c**) O (2p3/2), (**d**) Fe(2p), and (**e**) Cu(2p).

3.2.2. pH

As a key factor affecting the catalytic reaction, this experiment investigated the effect of initial pH of aqueous solution (3–11) on HA removal by FeCu@BC (5.0 g/L). As shown in Figure 5b, the removal efficiency of HA remained above 95% at a pH of 3–7. HA was almost completely removed at pH 3 within the first 30 min. This was mainly attributed to the accelerated precipitation of metal ions under acidic conditions, which promoted the catalytic reaction through the enhancement of the production of free radicals [42]. When the pH was increased from 7 to 11, the removal efficiency decreased significantly from 99.7% to 38.2%. At pH values close to 7, the HA removal efficiency was above 95%. However, when the pH was increased to 9, the removal efficiency of HA decreased significantly (61.3%). This was possibly caused by the fact that the metal hydroxides from the reaction between hydroxide in the solution and the metal ions on the surface of FeCu@BC settled on the catalyst surface, thus blocking the active sites for further reaction with HA [43]. Overall, FeCu@BC exhibited excellent catalytic oxidation performance, especially at neutral pH, opening the door to the possibility of using FeCu@BC to treat HA in secondary effluent of wastewater treatment plants (pH = 6–9). In the follow-up experiment, the pH condition was set to 6.8–7.5.

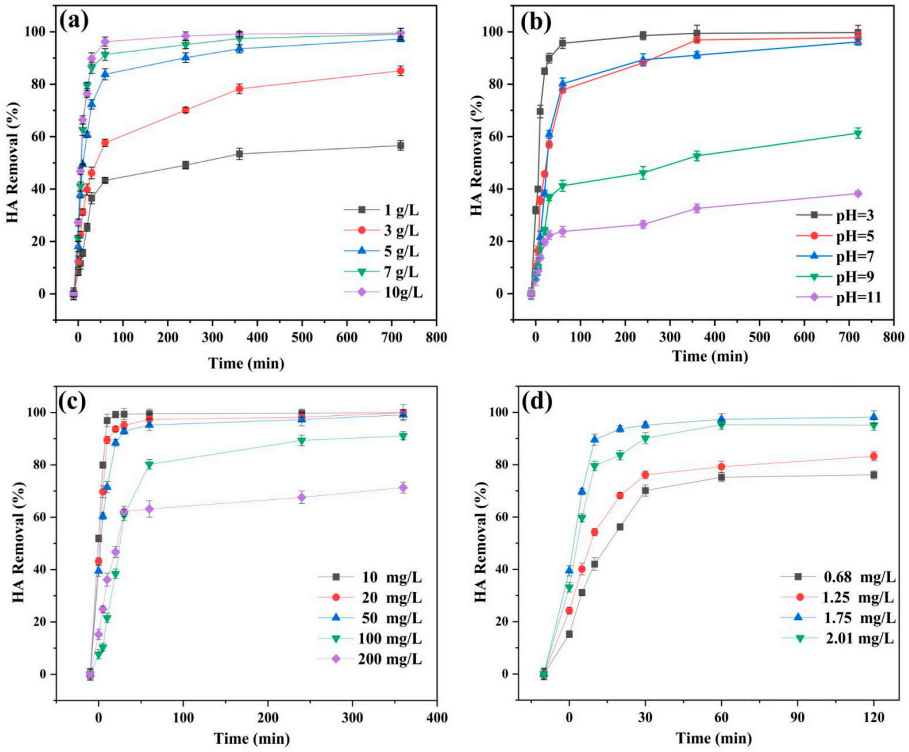

Figure 5. Effects of FeCu@BC dosage (**a**), initial solution pH (**b**), initial concentration (**c**), and DO concentration (**d**) on HA removal.

3.2.3. The Effect of Initial Concentrations

The effects of initial concentrations of HA (10 mg/L, 20 mg/L, 50 mg/L, 100 mg/L, and 200 mg/L) on HA removal by FeCu@BC (5.0 g/L) were investigated. As shown in Figure 5c, the HA removal efficiency decreased with increasing initial concentrations of HA. When the initial concentrations of HA were 10–50 mg/L, the HA removal efficiency was more than 90% within 30 min. As the HA concentration increased to 100 mg/L and 200 mg/L, the HA removal efficiency was only 91.1% and 71.3%, respectively, after 360 min of reaction. This, possibly, can be ascribed to the fact that the adsorption sites and active sites on the catalyst surface tended to be saturated at higher HA concentration, resulting in the continuously decreasing HA removal efficiency.

3.2.4. Effect of DO Concentration on HA Removal

In order to verify the effect of DO on the FeCu@BC catalyst, this experiment simulated the real situation of the secondary effluent of wastewater treatment plant through aeration. The correlation between the aeration flow rate and DO concentration during the experiment is shown in Table 3. With increasing DO concentrations, the removal efficiency of HA by FeCu@BC increased at first and then decreased (Figure 5d). Compared to the unaerated condition (DO concentration = 0.68 mg/L), the removal efficiency of HA increased by about 10% at a DO concentration of 1.25 mg/L. When the DO concentration increased to 1.75 mg/L, the removal efficiency of HA reached its highest (98.2%), a phenomenon ascribable to the increasing contact between HA and the FeCu@BC catalyst under the aeration condition. However, the HA removal efficiency decreased slightly (95.3%) at a DO concentration of 2.01 mg/L, mainly due to the large number of bubbles from excessive aeration which increased the mass transfer resistance of the reaction solution [44]. In actual water treatment, the suitable DO concentration (around 1.75 mg/L) in the secondary effluent could not only save energy, but also facilitate the removal of HA.

Table 3. Aeration flow rate and DO concentration during HA removal by the FeCu@BC catalyst system.

Aeration Flow Rate (L/min)	Volume (L)	Do Concentration (mg/L)
0.0	0.1	0.68
0.3	0.1	1.25
0.6	0.1	1.75
0.9	0.1	2.01

3.2.5. Influence of Coexistence of Inorganic Ions

In the actual water treatment process, the aqueous system contains a large number of inorganic anions and cations at the same time, among which some ions might have different effects on the catalytic oxidation reaction. Given the widespread presence of inorganic ions (NO_3^-, Cl^-, SO_4^{2-} and PO_4^{3-}) in the secondary effluent water [47], their effects on HA removal by FeCu@BC were investigated (Figure 6). The HA removal by FeCu@BC catalysts did not change significantly even at higher concentrations of NO_3^- and Cl^- (10–50 mg/L). When the SO_4^{2-} concentration increased from 10 mg/L to 50 mg/L, the removal of HA by FeCu@BC catalysts was significantly inhibited. It was probably because of the combination of SO_4^{2-} with iron and copper ions [48]. However, the removal of HA by FeCu@BC catalysts improved at 0.1–1.0 mg/L PO_4^{3-}. This change might be due to the fact that the phosphate in the solution could prevent the Fe^{2+} from being oxidized by the OH (Equation (3)), thus ensuring the continuous transfer of electrons under neutral conditions [49].

$$Fe^{2+} + \cdot OH \rightarrow Fe^{3+} + OH^- \quad (3)$$

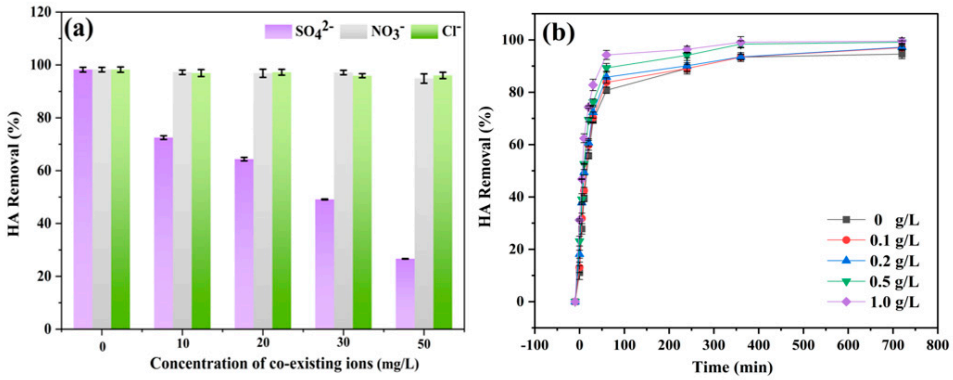

Figure 6. The effect of different anions on the degradation of HA in the FeCu@BC system. (**a**) SO_4^{2-}, NO_3^-, and Cl^-, and (**b**) PO_4^{3-}.

3.3. Identification of Active Species

In general, catalysts mainly produce radicals and non-radicals during the activation of free radicals [16]. The quenching experiments were implemented in order to evaluate the contribution of ROS to HA degradation in the FeCu@BC catalyst. As a hydrophilic scavenger, MEOH was generally used to concurrently quench the freely diffused •OH ($•OH_{free}$) in the solution, while TBA was more inclined to quench •OH [50]. Furthermore, NBA could quench the $•OH_{ads}$ present on the surface of the catalyst, which could comprehensively estimate the dedication of $•OH_{ads}$ and $•OH_{free}$. In addition, FFA could effectively quench $^1O_2$ [51]. As shown in Figure 7a, after adding TBA, MeOH, FFA, and NBA, the removal efficiencies of HA by the FeCu@BC catalyst decreased from 92.5% to 76.4%, 75.1%, 68.07%, and 80.3%, respectively. This result indicates that $•OH_{free}$ and $^1O_2$ free radicals were responsible for HA degradation, with $^1O_2$ being the dominant species (about 30% contribution). According to the results from the EPR experiments, there were four peaks in the presence of DMPO, with the ratio of 1:2:2:1 (from left to right) (Figure 7b). The characteristic triplet signal (1:1:1) of $^1O_2$ was captured by TEMP. In summary, radicals

(•OH) and non-radicals ($^1O_2$) coexisted in the FeCu@BC catalytic system. The predicted mechanism of ROS generation is shown in Equations (4)–(11). Three ROS (•OH, $^1O_2$, and $O_2^{\bullet-}$) were present throughout the process. In EPR signal, only two types of ROS (·OH and $^1O_2$) were captured, indicating that the content of $O_2^{\bullet-}$ was low and most of it was converted to $^1O_2$.

$$Fe^{2+} + O_2 + H \rightarrow Fe^{3+} + \bullet OH_{ads} + H_2O \quad (4)$$

$$Fe^{2+} + O_2 + H \rightarrow Fe^{3+} + \bullet OH_{free} + H_2O \quad (5)$$

$$Cu^0 + O_2 + H \rightarrow Cu^+ + \bullet OH_{ads} + H_2O \quad (6)$$

$$Cu^+ + O_2 + H \rightarrow Cu^{2+} + \bullet OH_{ads} + H_2O \quad (7)$$

$$Cu^+ + O_2 + H \rightarrow Cu^{2+} + \bullet OH_{free} + H_2O \quad (8)$$

$$Fe^{3+} + O_2 + OH^- \rightarrow Fe^{2+} + O_2^{\cdot -} + H_2O \quad (9)$$

$$O_2^{\cdot -} + H \rightarrow {}_1O_2^+ + H_2O_2 \quad (10)$$

$$Fe^{2+} + H_2O_2 \rightarrow Fe^{3+} + \bullet OH_{free} + OH^- \quad (11)$$

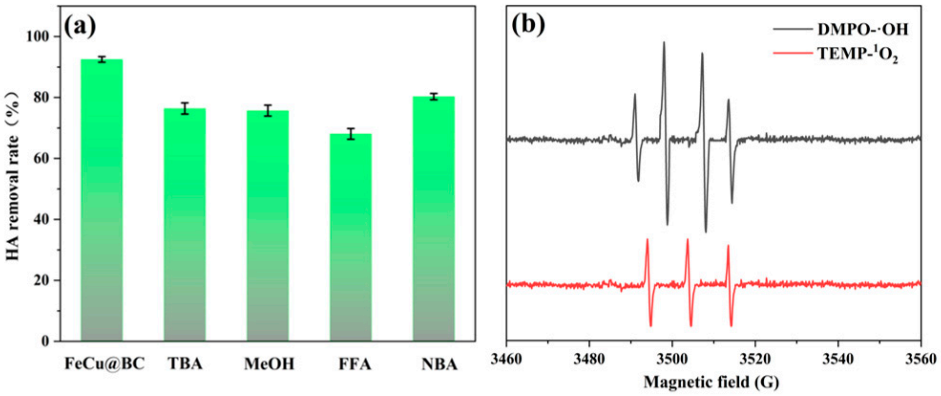

Figure 7. Quenching experiment (**a**) and ESR test results (**b**).

3.4. Changes in the Fluorescence Characteristics and Molecular Weight of HA

The 3D-EEMs were used to qualitatively characterize the changes in certain organic compounds in HA after catalytic oxidation treatment (Figure 8). An obvious peak located at Ex/Em of 278/422 (peak A) was characteristic of HA. As the reaction progressed, the total fluorescence intensity of HA decreased. After reacting with the FeCu@BC catalyst for 5 min, the fluorescence intensity of peak A significantly weakened and disappeared at 60 min.

$A_{254}/A_{254'}$ could reflect the changes in humic acid-like with macromolecular organic matter and aromatic compounds containing C=C double bonds and C=O double bonds in water [52]. The E_2/E_3 had been proved to be negatively correlated with the molecular weight. There was no significant change in E_2/E_3 (Figure 9a), suggesting that BC only removed HA by adsorption. As shown in Figure 9b, $A_{254}/A_{254'}$ decreased from 1 to 0.86 within 30 min during BC adsorption, and then there was no significant change, indicating that BC reached saturation [53]. In the FeCu@BC system, $A_{254}/A_{254'}$ decreased from 1 to 0.05, mainly because the humic acid-like with macromolecular organic matter and aromatic compounds containing C=C double bonds and C=O double bonds was oxidized by the FeCu@BC catalyst. As the extension of the reaction time, the molecular weight of the solution became smaller, further proving that the FeCu@BC catalyst broke the complex macromolecular structure of HA to form small molecules or CO_2 and H_2O.

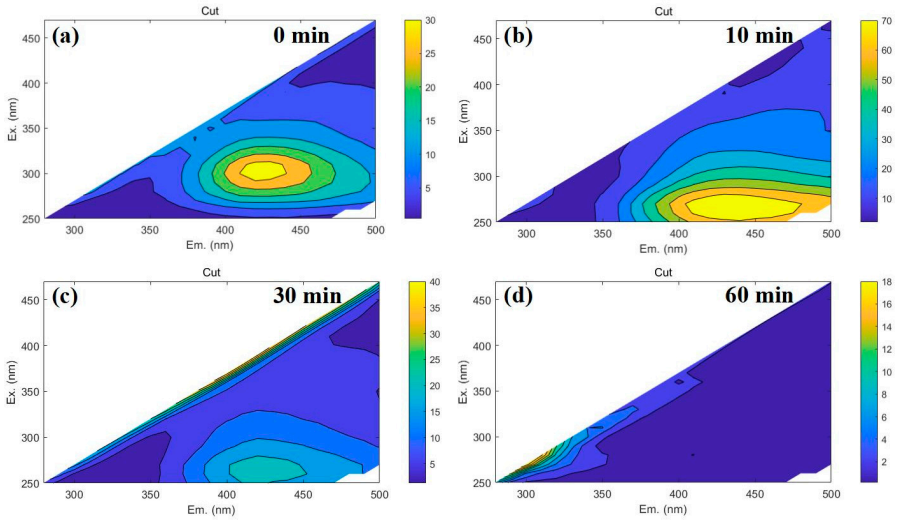

Figure 8. The EEM spectra of HA catalytic oxidation by the FeCu@BC over 0 min (**a**), 10 min (**b**), 30 min (**c**), and 60 min (**d**).

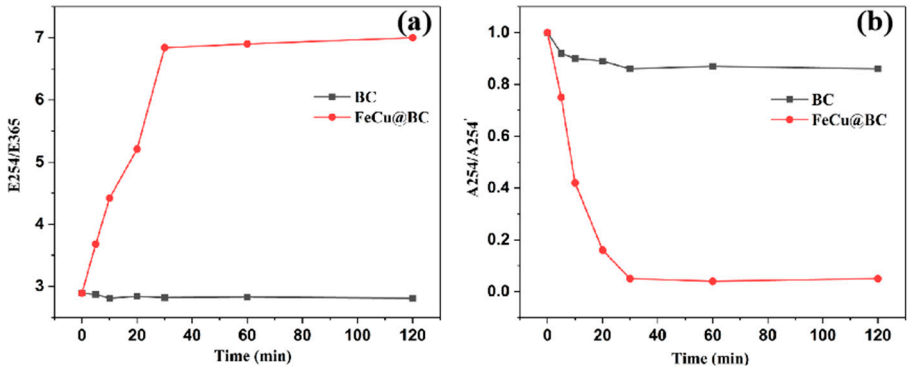

Figure 9. Changes in absorbance ratio (**a**) and molecular weight of HA_{254} (**b**) during the reaction process.

3.5. The Possible Catalytic Oxidation Mechanism

The surface elemental composition of the FeCu@BC catalyst at the end of the experiment is shown in Figure 4. At the end of the reaction, the new peaks at 282.09 eV and 286.36 eV indicated the presence of C–O and Carbide ratios on the surface of FeCu@BC catalysts (Figure 4a). This might be due to the oxidation of C=O as an electron transfer intermediate during the reaction and the formation of metal chelates by complexation of HA with metals. After the reaction with HA, the emerging peaks (282.09 eV and 286.36 eV) and the decrease in the C–C/C=O ratio (from 7.95 to 1.75) suggested the indication of a decrease in the C=O bonding and an increase in the ratio of C–O and Carbide, a phenomenon which may be attributed to the fact that the C=O was oxidized as an intermediate for the transfer of electrons in the course of the reaction and the generation of HA with the metal complexes to form metal chelates. The Fe 2p spectra of the FeCu@BC catalyst after the reaction showed that the Fe^{2+}/Fe^{3+} changed from 0.62 to 0.58, and the ratio of Fe^{2+} to Fe^{3+} did not change significantly (Figure 4c). Combined with the FTIR and Cu 2p XPS spectra, the decrease in O–H intensity on the surface of the FeCu@BC catalysts after reaction could be attributed to the electronic contribution of hydroxyl groups to promote the Fe (III) reduction [42]. The percentage of Cu^{1+} and Cu^{2+} increased significantly after the reaction (Figure 4d), further demonstrating the conversion of Cu^0 into Cu^{1+} and Cu^{2+} during the degradation process, and the electron transfer during the conversion process promoted the interconversion of Fe^{2+} and Fe^{3+}.

In order to further show the mechanism of the FeCu@BC catalyst in the HA removal process, a DFT calculation was used to analyze the reactive sites and bond breaks of HA during the removal process. The structure optimization of HA was calculated using Gaussian 16 software, and atoms with reactive sites were indicated by numbers (Figure 10). It was reported that the electrophilic reaction in the chemical structure was closely related to its highest molecular orbital (HOMO), while the lowest unoccupied molecular orbital (LUMO) was related to the nucleophilic reaction [54]. According to the Fukui functional theory, higher values of f indicated that the atom is more susceptible to electrophilic attack ($^1O_2$), while higher values of f^0 suggested that the atom was more susceptible to a free radical attack (•OH) [55]. As shown in Figure 11, 1C, 4C, 16O, 23O, and 24O exhibited high f^0 values. The highest occupied molecular orbital (HOMO) represented the ability to lose electrons. The distribution of HOMO in HA was consistent with f^-, suggesting that the 1C, 4C, 19N, 16O, and 24O of the aromatic ring were more prone to lose electrons and be attacked by electrophilic species ($^1O_2$) [56]. In summary, the C=O bond of HA was more vulnerable to free radical attacks (•OH and $^1O_2$).

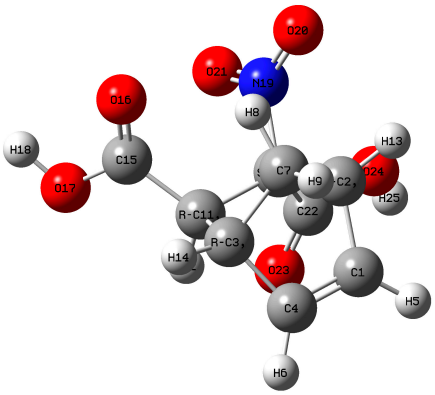

Figure 10. The structure optimization of HA.

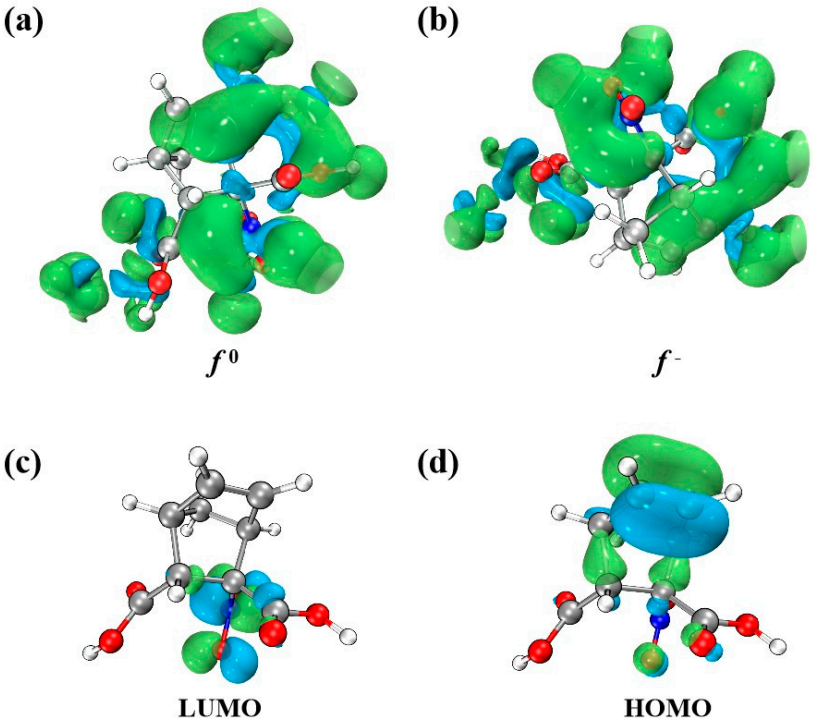

Figure 11. The gaussian calculation of HA. The contour surfaces of Fuku f^0 (**a**) and f^- (**b**) for HA; LUMO orbit (**c**) and (**d**) HOMO orbit of HA.

3.6. Variation in the Type and Yield of DBPs

In these experiments, the type and yield of chlorinated DBPs before and after the treatment with the FeCu@BC catalyst were investigated. The types and concentrations of DBPs are shown in Figure 12. Four DBPs, including trichloromethane (TCM), chloroacetic acids (MCAA), dichloroacetic acid (DCAA), and trichloroacetic acid (TCAA), were detected. After disinfection for 24 h, the generation of DBPs without treatment with the FeCu@BC catalyst was much higher than that associated with the treated sample. The highest concentration of TCAA among the four DBPs was probably caused by the conversion of MCAA and DCAA into TCAA due to longer sterilization time [57]. After treatment using the FeCu@BC catalyst, the TCM, MCAA, DCAA, and TCAA decreased by 68.8%, 49.2%, 45.8%, and 38.6%, respectively, compared to those without treatment. Obviously, the FeCu@BC catalyst could efficiently decrease the production of disinfection by-products produced by HA during chlorine disinfection.

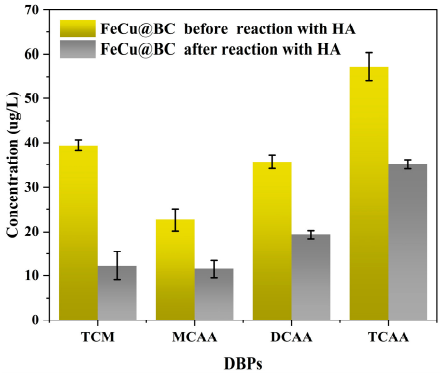

Figure 12. The amount of disinfection by-products produced before and after reaction with HA.

3.7. Reusability, Stability, and Applicability of FeCu@BC

In addition to the removal performance, reusability and stability are key factors affecting the practical application of catalysts. In this study, HA removal experiments with four consecutive cycles (initial pH 7) were used to evaluate the reusability of the catalyst. As shown in Figure 13a, HA was almost completely eliminated in the first cycle. After three cycles, HA removal could still be achieved up to more than 70%. In the 1st cycle, the highest leaching Fe and Cu concentrations were 0.30 mg/L and 0.80 mg/L, respectively, both of which were below the heavy metal emission limit of China (2.0 mg/L) (Figure 13b). By the 4th cycle, the leaching of Fe and Cu was almost undetectable. In summary, the FeCu@BC catalyst has high reusability, stability, and safety, and has great potential with respect to the removal of SMP from the tailwater of real wastewater plants to reduce the production of disinfection by-products and their toxicity in coastal and other aquatic environment.

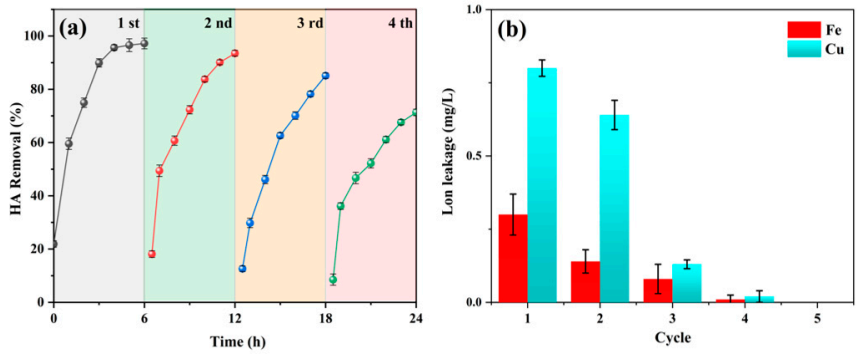

Figure 13. The reuse capacity of FeCu@BC catalysts (HA concentration = 100 mg/L, FeCu@BC loading = 0.5 g/L, and DO concentration = 1.75 mg/L) (**a**), and metal ion leakage of FeCu@BC catalyst during recycling (**b**).

3.8. Performance Comparison

In this research, the prepared FeCu@BC material was used to remove the large molecules of organic matter (HA). Based on the removal mechanism of catalytic oxidation, it can also be effective in treating other types of effluents, such as chlorinated hydrocarbons [58], tetracycline [59], and rhodamine B dye [60].We made a new Table 4 to compare the efficiency of FeCu@BC with other existing methods or catalysts used for similar purposes in wastewater treatment. As shown in Table 4, FuCu@BC exhibited a better removal efficiency than many other catalysts, particularly the FONC@PAC, MIL-53Fe@TiO_2, and $CuFeO_2$/NPC. Because the concentration of organic matter in the secondary effluent of the sewage plant is relatively low, the dosage of FeCu@BC will be higher, something which needs to be confirmed based on the actual water quality.

Table 4. Comparison of catalyst performance in related studies.

Catalyst	Contaminant Type	Removal Efficiency	Author
FONC@PAC	Tetracycline	0.02 mmol/g/min	[60]
Kaolinite/zero valent ironc	Bisphenol A	0.28 mmol/g/min	[61]
Yeast-supported Fe^0@Fe_2O_3	Tetracycline	0.21 mmol/g/min	[62]
$CuFeO_2$/NPC	Nimesulide	0.07 mmol/g/min	[63]
MIL-53Fe@TiO_2	Tetracycline	0.03 mmol/g/min	[64]
FeCu@BC	Humic acid	0.35 mmol/g/min	This study

3.9. Limitations and Future Research

Similarly to many studies, there are some limitations in this piece of work. Firstly, the water quality of wastewater is complex, and the characteristics of wastewater vary among industries. In the actual operation process, the selection and design of catalytic oxidation equipment need to be determined according to the specific conditions of the wastewater treatment plant. It is necessary to adjust and optimize the equipment with respect to the actual situation. Secondly, the catalyst is the key to the catalytic oxidation process and its performance directly affects the treatment effect. During the operation process, the catalyst may experience reduced activity, poisoning, and other issues, necessitating regular checks and replacements. Finally, the operation and maintenance costs associated with the catalytic oxidation process can be high, including catalyst replacement, equipment maintenance, and energy consumption. During operation, the relationship between cost and treatment effect needs to be considered. To guarantee the effectiveness of the catalytic oxidation process, it is essential to implement an appropriate monitoring system for the real-time monitoring and assessment of both influent and effluent water quality.

4. Conclusions

In this study, a simple one-step pyrolysis method was used to synthesize FeCu@BC, which was implemented for the removal of HA from secondary effluent as disinfection by-products precursors by CWAO under normal temperature and pressure. The results showed that the removal efficiency of HA reached a maximum of 93.2% when the FeCu@BC dosage, pH, initial HA concentration, and DO concentration were 5.0 g/L, 7, 100 mg/L, and 1.75 mg/L, respectively. The quenching experiments and EPR tests confirmed that •OH and $^1O_2$ free radicals played a role in the removal of HA. The FeCu@BC catalysts showed good reusability and stability, and the removal efficiency of HA was maintained at more than 70% after three cycles. In addition, the study performed chlorinated disinfection for the treated effluent, and the FeCu@BC catalyst reduced the yield of chlorinated DBPs from HA. In summary, usage of FeCu@BC material opens the door to the possibility of removing the precursors of disinfection by-products from secondary effluent of sewage treatment plant and DBPs after disinfection.

Author Contributions: Conceptualization, W.W., S.W. and H.Y.; methodology, W.W., S.W. and H.Y.; software, W.W. and H.Y.; validation, W.W., H.W., Y.L. and C.Z.; formal analysis, W.W., Y.L. and F.K.; investigation, W.W. and S.W.; data curation, W.W. and H.Y.; writing—original draft preparation, W.W.; writing—review and editing, W.W., S.W. and H.Y.; funding acquisition, F.K. All authors have read and agreed to the published version of the manuscript.

Funding: This study was supported by the National Natural Science Foundation of China (Grant No. 42277495) and the Natural Science Foundation of Shandong Province (ZR2020MD006).

Institutional Review Board Statement: Not applicable.

Informed Consent Statement: Not applicable.

Data Availability Statement: The data presented in this study are available from the corresponding author upon request.

Conflicts of Interest: The authors declare no conflict of interest.

References

1. Chen, X.F.; Yu, M.D.; He, X.S.; Zheng, M.X.; Xi, B.D.; Sun, Y.Y.; Fu, X.M.; Su, J. Fate of dissolved organic matter substructure in a full-scale wastewater treatment plant by using size exclusion chromatography multi-excitation-emission matrix analysis. *J. Clean. Prod.* **2021**, *328*, 129677. [CrossRef]
2. Li, J.; Wang, Z.W.; Wang, Y.Y. Integrating membrane aerated biofilm reactors with biological nitrogen removal processes: A new paradigm for achieving sustainable wastewater treatment plants. *Chem. Eng. J.* **2023**, *475*, 146025. [CrossRef]
3. Wang, Y.R.; Mauricius, M.D.S.; Ding, X.X.; Jérôme, L.; Bertrand, G.; Allen, S.S.; Jean-Philippe, C. Impact of EfOM in the elimination of PPCPs by UV/chlorine: Radical chemistry and toxicity bioassays. *Water. Res.* **2021**, *204*, 117634. [CrossRef]
4. Zheng, X.; Liu, T.; Guo, M.H.; Li, D.; Gou, N.; Cao, X.; Qiu, X.P.; Li, X.L.; Zhang, Y.Z.; Sheng, G.P.; et al. Impact of heavy metals on the formation and properties of solvable microbiological products released from activated sludge in biological wastewater treatment. *Water. Res.* **2020**, *179*, 115895. [CrossRef] [PubMed]
5. Ding, N.; Li, Z.W.; Jiang, L.; Liu, H.; Zhang, Y.P.; Sun, Y.X. Kinetics and mechanisms of bacteria disinfection by performic acid in wastewater: In comparison with peracetic acid and sodium hypochlorite. *Sci. Total. Environ.* **2023**, *878*, 162606. [CrossRef]
6. Zhang, J.Y.; Xu, Z.X.; Chu, W.H.; Ju, F.; Jin, W.; Li, P.; Xiao, R. Residual chlorine persistently changes antibiotic resistance gene composition and increases the risk of antibiotic resistance in sewer systems. *Water. Res.* **2023**, *245*, 120635. [CrossRef] [PubMed]
7. Sun, X.F.; Chen, M.; Wei, D.B.; Du, Y.G. Research progress of disinfection and disinfection by-products in China. *J. Environ. Sci.* **2019**, *81*, 52–67. [CrossRef]
8. Chen, T.T.; Wang, R.; Zhang, A.H.; Xu, T.; Xiao, R.; Chu, W.H.; Yin, D.Q. Peroxymonosulfate/chloride disinfection versus sodium hypochlorite disinfection in terms of the formation and estimated cytotoxicity of CXR-type disinfection by-products under the same dose of free chlorine. *Chem. Eng. J.* **2020**, *391*, 123557. [CrossRef]
9. Xue, B.U.; Yang, Q.; Jin, Y.S.; Zhu, Q.; Lan, J.Q.; Lin, Y.S.; Tan, J.S.; Liu, L.H.; Zhang, T.; Chirwa, E.M.N.; et al. Genotoxicity assessment of haloacetaldehyde disinfection byproducts via a simplified yeast-based toxicogenomics assay. *Environ. Sci. Technol.* **2023**, *57*, 16823–16833. [CrossRef]
10. He, H.; Sun, N.N.; Li, L.F.; Ai, J.; Zhou, H.; Yang, X.Y.; Yang, X.F.; Wang, D.S.; Zhang, W.J. Effects of dissolved organic matter removal and molecular transformation in different water treatment processes on formation of disinfection byproducts. *Water. Res.* **2023**, *245*, 120626. [CrossRef]
11. Sun, Y.Y.; Wang, Y.; Xue, N.; Yu, C.; Meng, Y.J.; Gao, B.Y.; Li, Q.L. The effect of DOM on floc formation and membrane fouling in coagulation/ultrafiltration process for treating TiO_2 nanoparticles in various aquatic media. *Chem. Eng. J.* **2017**, *16*, 429–437. [CrossRef]
12. Wang, P.; Ding, S.K.; Xiao, R.; An, G.G.; Fang, C.; Chu, W.H. Enhanced coagulation for mitigation of disinfection by-product precursors: A review. *Adv. Colloid Interface Sci.* **2021**, *296*, 102518. [CrossRef] [PubMed]
13. Chen, G.Q.; Wu, Y.H.; Fang, P.S.; Bai, Y.; Chen, Z.; Xu, Y.Q.; Wang, Y.H.; Tong, X.; Luo, L.W.; Wang, H.B.; et al. Performance of different pretreatment methods on alleviating reverse osmosis membrane fouling caused by soluble microbial products. *J. Membr. Sci.* **2022**, *641*, 119850. [CrossRef]
14. Li, J.Y.; Zheng, B.H.; Chen, X.; Li, Z.; Xia, Q.; Wang, H.; Yang, Y.; Zhou, Y.Y.; Yang, H. The Use of Constructed Wetland for Mitigating Nitrogen and Phosphorus from Agricultural Runoff: A Review. *Water* **2021**, *13*, 476. [CrossRef]
15. Lee, Y.J.; Jeong, Y.J.; Cho, I.S.; Lee, C.G.; Park, S.J.; Alvarez, P.J.J. The inhibitory mechanism of humic acids on photocatalytic generation of reactive oxygen species by TiO_2 depends on the crystalline phase. *Chem. Eng. J.* **2023**, *476*, 146823. [CrossRef]
16. Yang, H.J.; Lee, C.G.; Lee, J.C. Utilizing animal manure-derived biochar in catalytic advanced oxidation processes: A review. *J. Water. Process. Eng.* **2023**, *56*, 104545. [CrossRef]

17. Li, C.; Wang, Z.B.; Li, A.; Song, Z.L.; Ren, R.J.; Zuo, K.C.; Qi, F.; Ikhlaq, A.; Ismailova, O. Superior performance of catalytic ozonation on molecular-level transformation of effluent organic matter and self-cleaning property in catalytic ozonation membrane reactor. *Appl. Catal. B Environ.* **2023**, *338*, 122076. [CrossRef]
18. Feng, H.L.; Zhang, Z.J.; Kuang, Q.Y.; Chen, S.H.; Huang, D.; Zhou, X.W. The transformation of dissolved organic matter and formation of halogenated by-products during electrochemical advanced oxidation pretreatment for shale gas produced water. *J. Hazard. Mater.* **2023**, *455*, 131614. [CrossRef]
19. Ashish, S.; Arya, V. Effects of pharmaceuticals on membrane bioreactor: Review on membrane fouling mechanisms and fouling control strategies. *Sci. Total. Environ.* **2021**, *808*, 152132. [CrossRef]
20. Ding, Z.; Liu, C.; Yang, B.G.; Ding, C.; Mao, S.; Shi, M.X.; Hong, X.Y.; Wang, F.Y.; Xia, M.Z. The efficient degradation of high concentration phenol by Nitrogen-doped perovskite La_2CuO_4 via catalytic wet air oxidation: Experimental study and DFT calculation. *Sep. Purif. Technol.* **2023**, *322*, 124310. [CrossRef]
21. Teng, C.Y.; Zhou, K.G.; Liao, L.J.; Zhang, X.K.; Zhao, K.Q.; Korvayan, J.W.; Peng, C.H.; Chen, W. Coordination-driven Cu-based Fenton-like process for humic acid treatment in wastewater. *Sci. Total Environ.* **2022**, *838*, 156462. [CrossRef]
22. Cai, J.B.; Li, H.; Feng, K.; Cheng, Y.C.; He, S.; Masaki, T. Low-temperature degradation of humic acid via titanium zirconium oxide@copper single-atom activating oxygen: Mechanism and pathways. *Chem. Eng. J.* **2022**, *450*, 138239. [CrossRef]
23. Rajendra, G.; Anurag, G. Performance of heterogeneous catalytic wet oxidation for the removal of phenolic compounds: Catalyst characterization and effect of pH, temperature, metal leaching and non-oxidative hydrothermal reaction. *J. Environ. Chem. Eng.* **2017**, *5*, 468–478. [CrossRef]
24. Wang, H.Y.; Li, G.Q.; Zhang, S.T.; Li, Y.; Zhao, Y.L.; Duan, L.U.; Zhang, Y.F. Preparation of Cu-Loaded Biomass-Derived Activated Carbon Catalysts for Catalytic Wet Air Oxidation of Phenol. *Ind. Eng. Chem. Res.* **2020**, *59*, 2908–2920. [CrossRef]
25. Wang, A.Q.; Hou, J.; Xu, Q.C.; Wu, J.; Xing, B.S. Green synthesis of zero valent iron using tannins to activate persulfate for sulfamethoxazole degradation. *Environ. Pollut.* **2023**, *336*, 122418. [CrossRef]
26. Hassan, M.N.A.; Nabil, S.R.; Sherien, E.; Adewale, A. Copper ferrite immobilized on chitosan: A suitable photocatalyst for the removal of ciprofloxacin, ampicillin and erythromycin in aqueous solution. *Catal. Commun.* **2023**, *182*, 106745. [CrossRef]
27. Zhang, P.; Song, D.B.; Xue, J.X.; Hao, Y.L.; Shang, X.F.; Wang, C.P.; Tang, J.C.; Sun, H.W. Sulfidated zero valent iron as a persulfate activator for oxidizing organophosphorus pesticides (OPPs) in aqueous solution and aged contaminated soil columns. *Chemosphere* **2021**, *281*, 130760. [CrossRef]
28. Jun, L.; Yi, R.; Fang, Z.J.; Bo, L. Heterogeneous catalytic oxidation for the degradation of p-nitrophenol in aqueous solution by persulfate activated with $CuFe_2O_4$ magnetic nano-particles. *Chem. Eng. J.* **2017**, *324*, 63–73. [CrossRef]
29. Luo, H.H.; Yu, L.Q.; Xue, K.H.; Liu, C.; Ding, R.J.; Zhu, H.F.; Zhang, Y.P. Multilevel hollow hierarchical heterostructure with DB-IEF and space-confined effect for enhanced bifunctional PHE/HER activity. *Sep. Purif. Technol.* **2023**, *330*, 125373. [CrossRef]
30. Yang, Q.; Zhong, Y.F.; Zhang, Z.Q.; Dang, Z.; Li, F.B.; Zhang, L.J. Simultaneous degradation of sulfamethazine and reduction of Cr(VI) by flexible self-supporting Fe-Cu-Al_2O_3 nanofibrous membranes as heterogeneous catalysts: Insights into synergistic effects and mechanisms. *Sep. Purif. Technol.* **2023**, *472*, 144984. [CrossRef]
31. Xin, S.S.; Huo, S.Y.; Xin, Y.J.; Gao, M.C.; Wang, Y.H.; Liu, W.J.; Zhang, C.L.; Ma, X.M. Heterogeneous photo-electro-Fenton degradation of tetracycline through nitrogen/oxygen self-doped porous biochar supported $CuFeO_2$ multifunctional cathode catalyst under visible light. *Appl. Catal. B Environ.* **2022**, *312*, 121442. [CrossRef]
32. Li, Y.X.; Xu, D.F.; Lin, H.Z.; Wang, W.H.; Yang, H. Nutrient released characteristics of struvite-biochar fertilizer produced from concentrated sludge supernatant by fluidized bed reactor. *J. Environ. Manag.* **2022**, *325*, 116548. [CrossRef] [PubMed]
33. Wu, L.Y.; Xu, D.F.; Li, B.; Wu, D.; Yang, H. Enhanced removal efficiency of nitrogen and phosphorus from swine wastewater using MgO modified pig manure biochar. *J. Environ. Chem. Eng.* **2023**, *325*, 116548. [CrossRef]
34. Jin, X.; Du, X.H.; Liu, G.G.; Jin, B.H.; Cao, K.H.; Chen, F.Y.; Huang, Q. Efficient destruction of basic organo-nitrogenous compounds in liquid hydrocarbon fuel using ascorbic acid/H_2O_2 system under ambient condition. *J. Hazard. Mater.* **2023**, *459*, 132242. [CrossRef]
35. Chio, C.L.; Sain, M.; Qin, W.S. Lignin utilization: A review of lignin depolymerization from various aspects. *Renew. Sust. Energ. Rev.* **2019**, *107*, 232–249. [CrossRef]
36. Song, J.N.; Jin, P.K.; Jin, X.; Wang, X.C. Synergistic effects of various in situ hydrolyzed aluminum species for the removal of humic acid. *Water Res.* **2018**, *148*, 106–114. [CrossRef] [PubMed]
37. Mao, Y.X.; Liang, J.L.; Jiang, L.; Shen, Q.S.; Zhang, Q.; Liu, C.C.; Ji, F.Y. A comparative study of free chlorine and peroxymonosulfate activated by Fe(II) in the degradation of iopamidol: Mechanisms, density functional theory (DFT) calculations and formation of iodinated disinfection by-products. *Chem. Eng. J.* **2022**, *435*, 134753. [CrossRef]
38. Chinese National Environmental Protection Agency. *Water and Wastewater Monitoring Methods*, 4th ed.; Chinese Environmental Science Publishing Press: Beijing, China, 2002.
39. Wang, X.Y.; Wang, W.Y.; Wang, W.P.; Dong, L.; Zhai, T.Y.; Gao, Z.J.; Wang, K.; Wang, S.; Kong, F.L. Enhanced effect and mechanism of nanoFe-Ca bimetallic oxide modified substrate on Cu(II) and Ni(II)removal in constructed wetland. *J. Hazard. Mater.* **2023**, *456*, 131689. [CrossRef]
40. Lu, T.; Chen, F.W. Multiwfn: A multifunctional wavefunction analyzer. *J. Comput. Chem.* **2012**, *33*, 580–592. [CrossRef]

41. Qin, Y.X.; Zhang, L.Z.; An, T.C. Hydrothermal Carbon-Mediated Fenton-Like Reaction Mechanism in the Degradation of Alachlor: Direct Electron Transfer from Hydrothermal Carbon to Fe(III). *ACS Appl. Mater. Interfaces* **2017**, *9*, 17115–17124. [CrossRef]
42. Deng, J.M.; Zhang, C.; Zhao, J.; Cheng, Y.J.; Hou, K.J.; Zhang, L.H.; Fan, C.Z. Nanoscale zero-valent iron/biochar composite as an activator for Fenton-like removal of sulfamethazine. *Sep. Purif. Technol.* **2018**, *202*, 130–137. [CrossRef]
43. Xie, Y.R.W.; Guan, D.; Deng, Y.F.; Sato, Y.G.; Luo, Y.; Chen, G.H. Factors hindering the degradation of pharmaceuticals from human urine in an iron-activated persulfate system. *J. Environ. Sci.* **2024**, *135*, 130–148. [CrossRef] [PubMed]
44. Qi, H.Q.; Shi, X.L.; Liu, Z.B.; Yan, Z.H.; Sun, Z.R. In situ etched graphite felt modified with $CuFe_2O_4/Cu_2O/Cu$ catalyst derived from CuFe PBA for the efficient removal of sulfamethoxazole through a heterogeneous electro-Fenton process. *Appl. Catal. B Environ.* **2023**, *331*, 122722. [CrossRef]
45. Panagiota, T.; Nathalie, N.K.; Stefanos, M.; Katerina, K.; Urania, M.S.; Catherine, D.S. CuZn and ZnO Nanoflowers as Nano-Fungicides against *Botrytis cinerea* and *Sclerotinia sclerotiorum*: Phytoprotection, Translocation, and Impact after Foliar Application. *Materials* **2021**, *14*, 7600.
46. Çakmak, G.; Öztürk, T. Continuous synthesis of graphite with tunable interlayer distance. *Diam. Relat. Mater.* **2019**, *96*, 134–139. [CrossRef]
47. An, Y.L.; Ma, X.Y.; Chen, W.F.; Li, W.; Yang, S.Y.; Chen, R.C.; Wang, X.C. The impact of inorganic ions on the solar photolysis of chlorinated dissolved organic matter from different sources: Spectral characteristics, disinfection byproducts and biotoxicities. *J. Hazard. Mater.* **2023**, *451*, 131135. [CrossRef]
48. Zhong, W.L.; Peng, Q.; Liu, K.; Tang, X.K.; Zhang, Y.J.; Xing, J.J. Building $Cu^0/CuFe_2O_4$ framework to efficiently degrade tetracycline and improve utilization of H_2O_2 in Fenton-like system. *Chem. Eng. J.* **2023**, *474*, 145522. [CrossRef]
49. Lai, C.; Huang, F.L.; Zeng, G.M.; Huang, D.L.; Qin, L.; Cheng, M.; Zhang, C.; Li, B.S.; Yi, H.; Liu, S.Y.; et al. Fabrication of novel magnetic $MnFe_2O_4$/bio-char composite and heterogeneous photo-Fenton degradation of tetracycline in near neutral pH. *Chemosphere* **2019**, *224*, 910–921. [CrossRef]
50. Wang, L.L.; Lan, X.; Peng, W.L.; Wang, Z.H. Uncertainty and misinterpretation over identification, quantification and transformation of reactive species generated in catalytic oxidation processes: A review. *J. Hazard. Mater.* **2021**, *408*, 124436. [CrossRef]
51. Zhou, L.; Wu, Y.H.; Zhou, Y.Q.; Zhang, Y.L.; Xu, H.; Jang, K.S.; Dolfing, J.; Spencer, R.G.M.; Jeppesen, E. Terrestrial dissolved organic matter inputs drive the temporal dynamics of riverine bacterial ecological networks and assembly processes. *Water Res.* **2024**, *249*, 120955. [CrossRef]
52. Zhang, Y.T.; Liu, C.; Xu, B.B.; Qi, F.; Chu, W. Degradation of benzotriazole by a novel Fenton-like reaction with mesoporous Cu/MnO_2: Combination of adsorption and catalysis oxidation. *Appl. Catal. B Environ.* **2016**, *199*, 447–457. [CrossRef]
53. Yu, J.J.; Xu, H.; Yang, X.F.; Sun, H.Y.; Jin, Z.Y.; Wang, D.S. Floc formation and growth during coagulation removing humic acid: Effect of stirring condition. *Sep. Purif. Technol.* **2022**, *302*, 122084. [CrossRef]
54. Huang, Y.C.; Lai, L.D.; Huang, W.F.; Zhou, H.Y.; Li, J.; Liu, C.; Lai, B.; Li, N.W. Effective peroxymonosulfate activation by natural molybdenite for enhanced atrazine degradation: Role of sulfur vacancy, degradation pathways and mechanism. *J. Hazard. Mater.* **2022**, *435*, 128899. [CrossRef] [PubMed]
55. Tang, R.D.; Zeng, H.; Deng, Y.C.; Xiong, S.; Li, L.; Zhou, Z.P.; Wang, J.J.; Tang, L. Dual modulation on peroxymonosulfate activation site and photocarrier separation in carbon nitride for efficient photocatalytic organics degradation: Efficacy and mechanism evaluation. *Appl. Catal. B Environ.* **2023**, *336*, 122918. [CrossRef]
56. Ma, Y.X.; Zhao, K.; Wang, D.D.; Guo, J.F.; Wei, X.; Yang, W.J.; Zhao, J.Q.; Li, Z.Y. $MnFe_2O_4$ composited polyvinylidene fluoride catalytic ultrafiltration membrane via peroxymonosulfate activation for humic acid treatment: Exploration of synergistic mechanisms. *Sep. Purif. Technol.* **2023**, *332*, 125708. [CrossRef]
57. Senesi, N. Molecular and quantitative aspects of the chemistry of fulvic acid and its interactions with metal ions and organic chemicals. *Anal. Chim. Acta* **1990**, *232*, 77–106. [CrossRef]
58. Fan, B.; Zhou, B.N.; Chen, S.; Zhu, F.X.; Chen, B.; Gong, Z.M.; Wang, X.L.; Zhu, C.Y.; Zhou, D.M.; He, F.; et al. Preparation of Fe/Cu bimetals by ball milling iron powder and copper sulfate for trichloroethylene degradation: Combined effect of FeSx and Fe/Cu alloy. *Crystengcomm* **2023**, *460*, 132402. [CrossRef]
59. Wang, Y.; Qiao, L.L.; Zhang, X.Y.; Liu, Z.L.; Li, T.L.; Wang, H.T. Green synthesis of FeCu@biochar nanocomposites through a mechanochemical method for enhanced tetracycline degradation via peroxymonosulfate activation. *Sep. Purif. Technol.* **2024**, *328*, 125077. [CrossRef]
60. Shen, Y.H.; Xiao, Y.X.; Zhang, H.J.; Fan, H.J.; Li, Y.; Yan, Z.L.; Zhang, W.H. Synthesis of magnetic biochar-supported Fe-Cu bimetallic catalyst from pulp and paper mill wastes for the Fenton-like removal of rhodamine B dye. *Chem. Eng. J.* **2023**, *477*, 146823. [CrossRef]
61. Li, C.Q.; Yang, S.S.; Bian, R.Z.; Tan, Y.; Zhang, X.W.; Zheng, S.L. Efficient catalytic degradation of bisphenol A coordinated with peroxymonosulfate via anchoring monodispersed zero-valent iron on natural kaolinite. *Chem. Eng. J.* **2022**, *448*, 137746. [CrossRef]
62. Li, B.; Li, C.X.; Wang, Y.; Xu, W.Y.; Cui, K.P.; Zhan, X.Y.; Deng, R.; Zhang, X. In-situ preparation of yeast-supported $Fe^0@Fe_2O_3$ as peroxymonosulfate activator for enhanced degradation of tetracycline hydrochloride. *Chemosphere* **2023**, *324*, 138340. [CrossRef] [PubMed]

63. Xin, S.S.; Ma, B.G.; Zhang, C.L.; Ma, X.M.; Xu, P.; Zhang, G.S.; Gao, M.C.; Xin, Y.J. Catalytic activation of peroxydisulfate by alfalfa-derived nitrogen self-doped porous carbon supported $CuFeO_2$ for nimesulide degradation: Performance, mechanism and DFT calculation. *Appl. Catal. B Environ.* **2021**, *294*, 120247. [CrossRef]
64. Li, D.; Li, H.M.; Long, M.Y.; Bai, X.J.; Zhao, Q.Q.; Wen, Q.; Song, F. Synergetic effect of photocatalysis and peroxymonosulfate activation by MIL-53Fe@TiO_2 on efficient degradation of tetracycline hydrochloride under visible light irradiation. *Crystengcomm* **2022**, *24*, 4283–4293. [CrossRef]